Catalysis Science & Technology



PAPER

View Article Online
View Journal



Cite this: DOI: 10.1039/d4cy00270a

Nanosheet assembled microspheres of metal (Zn, Ni, and Cu) indium sulfides for highly selective CO₂ electroreduction to methane†

Schindra Kumar Ray,^a Rabin Dahal,^a Moses D. Ashie,^a Gayani Pathiraja^b and Bishnu Prasad Bastakoti ®**

Herein, metal indium sulfides (ZnIn₂S₄, NiIn₂S₄, and CuInS₂) were synthesized using a hydrothermal method. Nanosheet-assembled microspheres were observed. According to cyclic voltammetry, CuInS₂ revealed 19 and 6-fold current density enhancement compared to ZnIn₂S₄ and NiIn₂S₄, respectively. Also, linear sweep voltammetry results suggested a higher current density of CuInS₂ than the others. The lowest Tafel plot of CuInS₂ (189.15 mV dec⁻¹) suggested the improvement of electrocatalytic activity compared to those of Znln₂S₄ (282.53 mV dec⁻¹) and Niln₂S₄ (247.32 mV dec⁻¹). An H-type cell was used for selective electrochemical reduction of CO2 into CH4. The gaseous and liquid products were analyzed by gas chromatography and ¹H NMR, respectively. A higher Faraday efficiency (FE) was observed in CuInS₂ (80.11%) compared to those in ZnIn₂S₄ (67.78%) and NiIn₂S₄ (75.31%) towards the electrocatalytic reduction of CO₂ into methane (CH₄) at -0.6 V vs. RHE. A higher turnover frequency (TOF) value was observed in CulnS₂ compared to those in the other catalysts. CulnS₂ demonstrated remarkable stability, with neither an obvious current drop nor large FE fluctuation for 20 h during electrochemical CO2 reduction into CH4, indicating a superior electrocatalytic performance. The higher electrochemical performance of CulnS2 is associated with a larger BET surface area/electrochemical surface area, rich structural design, and abundant active sites. This work indicates a promising strategy for developing a ternary electrocatalyst for highly selective electrochemical reduction of CO2 to CH4.

Received 28th February 2024, Accepted 27th June 2024

DOI: 10.1039/d4cy00270a

rsc.li/catalysis

Introduction

An increase in CO₂ emission levels to the atmosphere by the rapid depletion of fossil fuels has led to the energy crisis and global warming. Such problematic issues can be mitigated by converting CO2 to value-added carbon-based fuels and chemical feedstock. Among various approaches, electrochemical CO2 reduction is inexpensive, abundant, and environmentally friendly and can be performed under ambient temperature and pressure.1-4 The electrochemical redox reaction consists of multiple proton/electron-transfer steps that can produce various types of C₁-C₃ gaseous or liquid products. Among different hydrocarbon products during the electrochemical CO₂ reduction reaction (CO₂RR), methane (CH₄) is the most valuable C1 product because of its compatibility with the current natural

infrastructure.⁵ In addition, the displacement of conventional CH₄ fuel production globally by the electrochemical CO₂RR technique can significantly contribute to a net zero CO₂ emission economy. Unfortunately, electrocatalytic conversion of CO₂ into CH₄ suffers from slow kinetics *via* multiple electron transfer. Therefore, it is necessary to design an efficient electrocatalyst for selective electrocatalytic reduction of CO₂ into CH₄.

Nowadays, various electrocatalysts (nanotwinned Cu,⁵ Cu-MOF,⁶ Cu-porphyrin,⁷ C/Pt,⁸ Cu/CeO₂,⁹ Zn atoms¹⁰ etc.) have been applied for selective electrochemical reduction of CO₂ into CH₄. However, precious metals, metal oxides, and MOF-based catalysts suffer from complicated synthesis processes, high cost, catalytic agglomeration, high rate of electrolysis,⁹ changes in active phases, element dissolution, and low electrochemical stability.¹ To solve these issues, a ternary metal indium sulfide is a perfect option because the synergistic effect of metal and indium atoms facilitated greater affinity between cations in metal indium sulfides and CO₂ molecules and thus resulted in enhanced electrocatalytic performances.¹¹ Also, metal indium sulfides are non-toxic, and have excellent physical/chemical stability, great durability, abundant metal vacancies, and In–S covalency that

^a Department of Chemistry, North Carolina A & T State University, 1601 E Market St, Greensboro, NC 27411, USA. E-mail: bpbastakoti@ncat.edu

^b Department of Nanoscience, Joint School of Nanoscience & Nanoengineering, University of North Carolina at Greensboro, Greensboro, North Carolina 27401,

[†] Electronic supplementary information (ESI) available: SEM, BET, XRD, electrochemical characterization. See DOI: https://doi.org/10.1039/d4cy00270a

may greatly enhance electrocatalytic performance. 12-14 In addition, metals tend to alter the coordination environment of indium sulfide, which may increase the electrocatalytic properties.14 Among various metals, Zn, Ni, and Cu revealed superior electrochemical CO₂RR ability. These metals are lowcost and have well-defined structures, high surface to volume ratio, and great selectivity. 6,15,16

Recently, Cai et al. and Chi et al. fabricated ZnIn2S4 for electrocatalytic reduction of CO2 into ethanol and formate, respectively. 11,14 However, the electrocatalytic CO2 reduction properties of NiIn2S4 and CuInS2 catalysts as well as selective electrocatalytic reduction of CO2 into CH4 have rarely been reported. Besides catalysts, good morphology can greatly promote electrocatalytic performances. Two dimension (2D) nanosheet assembled microspheres not only provide a large surface area and prevent the aggregation of active sites but also lower the contact resistance and thus enhance the electrocatalytic performance via efficient electron transfer.11 The rich defects and abundant active sites of metal indium sulfide could lower the reaction barrier, which can effectively reduce CO2 to hydrocarbons electrocatalytically.¹⁷ Also, sulphur sites of metal indium sulfides have low hydrogen absorption free energy and act as a promotor to enhance hydrocarbon products. 4 So, nanosheet assembled microsphere catalysts (ZnIn₂S₄, NiIn₂-S₄, and CuInS₂) are perfect options for selective electrocatalytic CO2 reduction into CH4.

In this work, ZnIn₂S₄, NiIn₂S₄, and CuInS₂ were synthesized using a hydrothermal method. The catalysts were well characterized by various techniques. Various electrochemical measurements (cyclic voltammetry, electrochemical impedance spectroscopy, linear sweep voltammetry, Tafel plot, and chronoamperometry) of ZnIn2-S₄, NiIn₂S₄, and CuInS₂ were carried out on an H-type cell. The stability of catalyst towards the electrocatalytic CO₂RR for 20 h was performed. The gaseous and liquid products were investigated by gas chromatography (GC) and ¹H NMR, respectively. The faradaic efficiencies (FEs) towards selective reduction of CO2 into CH4 were calculated at -0.6 V vs. RHE. Turnover frequency (TOF) was calculated for all catalysts. Possible mechanisms were explained.

Experimental section

Materials

The chemicals used throughout all experiments are of analytical grade and do not need any further purification. Zinc nitrate hexahydrate [Zn(NO₃)₂·6H₂O] (Alfa Aesar, LOT: R29E001, India), nickel(II) nitrate hexahydrate [Ni(NO₃)₂·6H₂-O] (Honeywell, lot no.: 12220, US), copper(II) nitrate trihydrate [Cu(NO₃)₂·3H₂O] (Acros Organics, lot: A0412121, Poland), indium(III) chloride tetrahydrate (InCl₃·4H₂O) (Sigma Aldrich, USA), and thioacetamide (TAA) (C2H5NS) (Sigma Aldrich, Switzerland) were used for the synthesis of the catalysts. Potassium bicarbonate (KHCO3) (Sigma Aldrich, Spain) was used as an electrolyte.

Synthesis of ZnIn₂S₄, NiIn₂S₄ and CuInS₂

A hydrothermal process was used to synthesize ZnIn₂S₄, $NiIn_2S_4$, and $CuInS_2$. In this process, 0.5×10^{-2} moles of Zn(NO₃)₂·6H₂O were dissolved in 30 mL deionized water. In addition, 0.5×10^{-2} moles of InCl₃·4H₂O and 10^{-2} moles of TAA were placed in 30 mL water. These solutions were magnetically stirred until a clear solution was formed. Then, the resulting solutions were mixed and magnetically stirred for 4 h. After stirring, the suspension was transferred into a Teflon-lined stainless-steel autoclave with a capacity of 100 mL. Afterward, the autoclave was shielded and maintained at 180 °C/14 h. The obtained yellow precipitate was washed with water and ethanol several times. It was dried in an oven and ZnIn₂S₄ yellow powder was obtained. Ni(NO₃)₂·6H₂O (0.5 × 10^{-2} moles) and Cu(NO₃)₂·3H₂O (0.5 × 10^{-2} moles) were used to synthesize NiIn₂S₄ and CuInS₂ powders, respectively. These powders were used for further characterization and electrochemical measurements. ZnIn₂S₄, NiIn₂S₄, and CuInS₂ were coded as ZIS, NIS, and CIS, respectively.

Material characterization

X-ray diffraction (XRD) patterns of the samples were obtained using a Rigaku Miniflex 600 (Japan) with Cu Ka radiation $(2\theta$: 20 to 80°, continuous rate: 4° per minute, and step: 0.02). The morphology of the samples was obtained by field emission scanning electron microscopy (FESEM, JEOL, JSM-IT800). The EDS elemental mapping/spectrum was obtained using an Oxford instrument. Transmission electron microscopy (TEM), and high-resolution (HRTEM) images of the samples were obtained using a JEOL JEM-2100 plus at 120 kV. X-ray photoelectron spectroscopy (XPS) of the samples was measured on a Thermo Scientific ESCALAB™ XI (Al Ka and 200 eV). The Brunauer-Emmett-Teller (BET) surface area and pore size distribution of samples were obtained from a NOVA 2200e (surface area and pore size analyzer). The analysis of gaseous products was performed by gas chromatography (GC) (SRI 8610C). Electrochemical characterization was performed on a CH instrument. The nuclear magnetic resonance (NMR) spectroscopy of the liquid product was investigated on an Ascend™ 400, Bruker.

Electrochemical measurements

The CH Instrument was used for measuring the electrochemical properties using a typical three-electrode system (counter electrode: platinum, reference electrode: Ag/ AgCl, and working electrode: ZIS, NIS, and CIS). For the electrolyte in electrochemical measurements, KHCO₃ (0.5 M) was used. For the preparation of working electrodes, 0.5 mL of C₂H₅OH, 50 µL Nafion, and 4 mg of powder samples were mixed and sonicated for 4 h. As a substrate, FTO glass (MSE 2.2 mm, 12-15 ohm sq⁻¹, TEC 15 coated glass substrates) was washed with water/ethanol for 1 h under ultrasonication. It was dried at 70 °C for 4 h in a vacuum oven. The well-dispersed ink was put in the glass substrate by controllable drop casting techniques. The available

working area was 1 cm 2 in the glass electrode. Then, it was dried in an oven (70 $^{\circ}$ C/4 h).

CO₂ gas (99.999%) was continuously passed in the H-type cell for saturation of the electrolyte for 40 min at 6 sccm. A mass flow controller (MC-100SCCM-D, Alicat Scientific) was used to regulate the flow rate of CO₂. To find the gaseous/liquid hydrocarbon products, the GC was equipped with a flame ionization detector (FID). For calibration, standard gas mixtures (ARC3) were applied under 1 atm and 298 K. Amperometry (i-t) measurements were performed at -0.6 V νs . RHE. The injection of gas in the GC was performed during the electrochemical CO₂RR. The concentration of gases in ppm was observed and faradaic efficiencies (FEs) were calculated. For electrocatalytic stability, the potential was applied at -0.6 V νs . RHE for 20 h. In addition, turnover frequency (TOF) was calculated for all samples using the following equation. ¹⁸

$$TOF = \frac{Q \times FE}{nF} / \frac{m \times w\%}{M \times t}$$

where Q, FE, F, n, m, w%, M, and t represent the total charge during chronoamperometry, faradaic efficiency, Faraday constant, number of electrons exchanged for the CH_4 formation, mass of the materials loaded on the working electrode, weight% of the catalyst from EDS, molecular weight of the materials, and time for the TOF unit, respectively.

Results and discussion

XRD diffraction spectra of the ZIS, NIS, and CIS samples are presented in Fig. 1. The XRD pattern of ZIS could be perfectly indexed to the pure hexagonal phase of $ZnIn_2S_4$ (JCPDS no. 65-2023). ^{17,19} In addition, all diffraction peaks of NIS were matched with the cubic spinel structure of $NiIn_2S_4$ (JCPDS no. 70-2900). ^{20,21} Also, the tetragonal phase of $CuInS_2$ (JCPDS

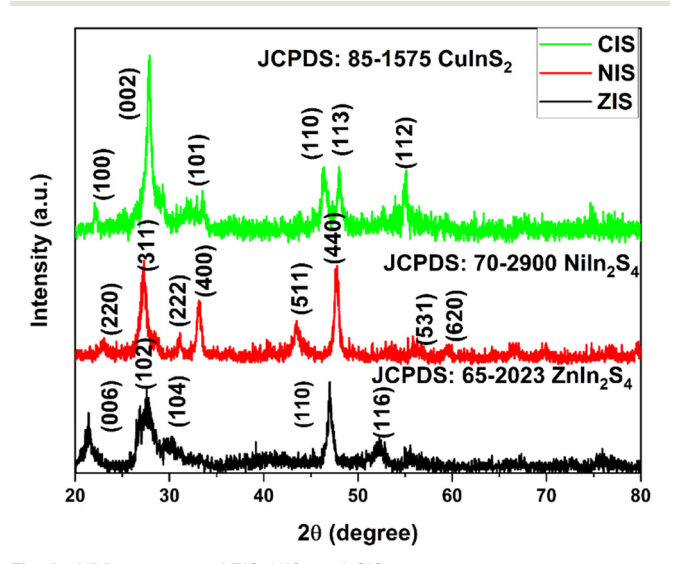


Fig. 1 XRD patterns of ZIS, NIS, and CIS.

no. 85-1575) was found in the CIS sample. 22,23 A lack of an impurity phase was observed in ZIS, NIS, and CIS samples successfully indicating fabrication of pure crystalline $ZnIn_2S_4$, $NiIn_2S_4$, and $CuInS_2$.

FESEM, TEM, and HRTEM images were performed to observe the morphologies and structures of ZIS, NIS, and CIS (Fig. 2 and 3). According to Fig. 2a, flower-like microspheres with a particle size of 2-10 µm were observed in ZIS particles which were composed of petal-like nanosheets. In addition, some hollow microspheres were clearly seen. NIS also revealed flower-like microspheres (2-7 µm) with a typical network structure/cavity containing various self-assembled nanosheet units (Fig. 2b). The microspheres of NIS were slightly distorted and agglomerated. As shown in Fig. 2c, microspheres (2 µm) were clearly observed. However, most of the microspheres were fused, and were assembled with nanosheets. Various big cavities were clearly found as compared to ZIS and NIS. These cavities along with the interconnected nanosheet in microspheres facilitate electron and electrolyte migration on the surface of the catalysts, which is beneficial for boosting the electrochemical performances towards the electrocatalytic CO₂RR. The possible reason for the formation of nanosheet assembled microsphere metal indium sulfides may be associated with the interaction of metals (Zn, Ni, and Cu) and In³⁺ cations as well as S²⁻ anions with H₂O. Due to this process, metal indium sulfide nuclei are produced. Also, excess TAA may attach to the surface of newly formed crystals, which can prevent the growth of the crystal shape. 24,25 Then, metal

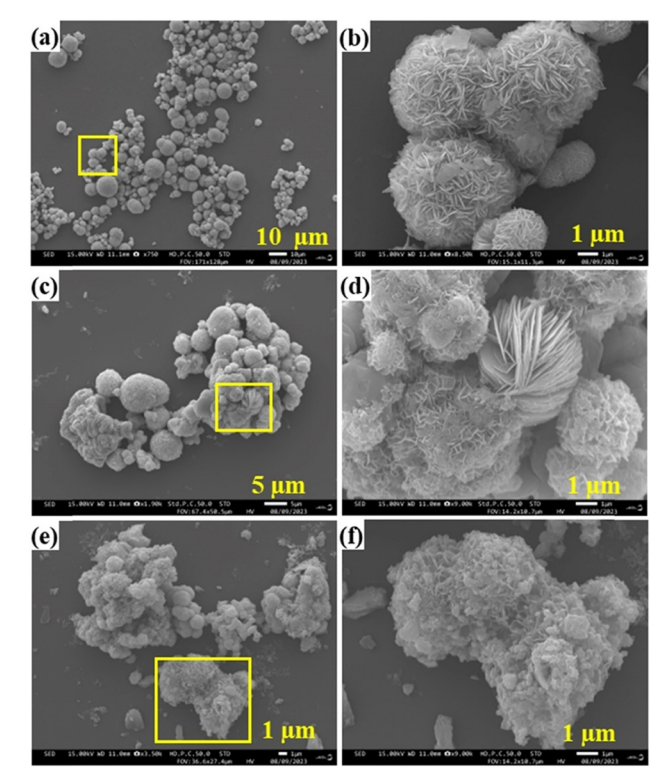


Fig. 2 FESEM images of ZIS (a and b), NIS (b and c), and CIS (d and e). The yellow-colored box indicates the magnified part.

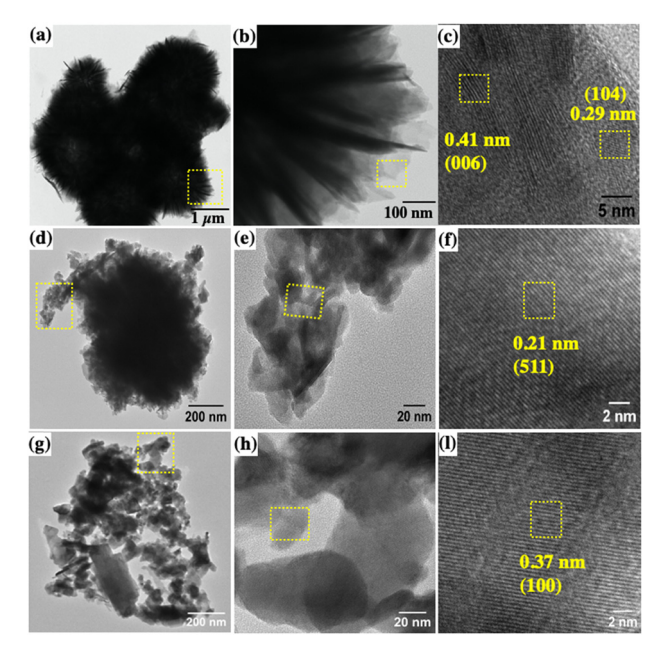


Fig. 3 TEM images (ZIS: a and b, NIS: d and e, and CIS: g and h) and HRTEM images (ZIS: c. NIS: f. and CIS: i). The vellow-colored dotted box indicates the magnified part.

indium sulfide nuclei grew into nanosheets and selfassembled to form flower-like microspheres which were driven by surface tension at high temperature during hydrothermal treatment.26 Furthermore, FESEM elemental mapping and spectra of ZIS, NIS, and CIS suggested the existence and uniform distribution of Zn, Ni, Cu, In, and S in the samples (Fig. S1 and S2†).

The morphologies/structures of ZIS, NIS, and CIS were further investigated by TEM and HRTEM images (Fig. 3). TEM images show that the microsphere is composed of many nanosheets, which was consistent with FESEM images. The magnified part of the TEM images is shown in Fig. 3b, e and h. The HRTEM image of ZIS showed a lattice spacing of 0.41 nm and 0.29 nm, corresponding to the (006) and (104) planes of ZnIn₂S₄, respectively (Fig. 3c). In addition, HRTEM images of NIS and CIS images indicate the spacing of the distinct lattice fringes with 0.21 nm and 0.37 nm, which can be indexed to the (511) and (100) planes of NiIn₂S₄ and CuInS₂, respectively (Fig. 3f and i). These planes were well matched with XRD patterns of the samples, suggesting the construction of pure ZnIn₂S₄, NiIn₂S₄, and CuInS₂ catalysts. Fig. S3† presents the N2 adsorption-desorption isotherms of ZIS, NIS, and CIS. All samples showed a type IV isotherm, that indicates the nature of mesoporous materials. The surface area of ZIS, NIS, and CIS was 47.76, 253.32, and 280.48 m² g⁻¹, respectively. CIS exhibited a higher surface area than the others. Meanwhile, the pore-size distribution curves further verify the mesoporous structures in ZIS, NIS, and CIS (Fig. S4†). The mesopores were centred at 27-50 nm. So, the large surface area and porous structures could provide a large electrochemically active surface area on electrocatalysts for fast ion and charge transport as well as abundant surface active/adsorption sites that may enhance the electrochemical CO₂RR.^{27,28}

To find the electronic chemical states of ZIS, NIS, and CIS, XPS was employed (Fig. 4). Zn 2p peaks are centred at 1022.36 eV and 1045.45 eV which can be assigned to the $2p_{3/2}$ and 2p_{1/2} orbitals, respectively (Fig. 4a). As shown in Fig. 4a, the binding energy difference is about 23.09 eV, which suggests the presence of Zn2+ in ZIS. 13,29,30 According to Fig. 4d, Ni 2p_{3/2} and Ni 2p_{1/2} peaks were located at 856.64 eV and 875.32 eV, respectively. In addition, satellite Ni 2p3/2 and Ni 2p_{1/2} peaks were observed at 862.45 eV and 883.03 eV, respectively. These results suggest the existence of Ni2+ in NIS. 20,31-33 The Cu 2p core level was deconvoluted into two peaks representing Cu 2p_{3/2} (931.61 eV) and Cu 2p_{1/2} (951.47 eV), suggesting the valence state of ions is +1 in CIS (Fig. 4g).³⁴ The In 3d spectra can be deconvoluted into 3d_{5/2} (ZIS: 445.43 eV, NIS: 446.31 eV, CIS: 444.71 eV) and 3d_{3/2} signals (ZIS: 453.07 eV, NIS: 453.93 eV, CIS: 452.26 eV). This result suggests the presence of In3+ in samples (Fig. 4b, e and h).21 The S 2p revealed 2p_{3/2} (ZIS: 162.10 eV, NIS: 162.97 eV, CIS: 162.23 eV) and 2p_{1/2} (ZIS: 163.40 eV, NIS: 165.50 eV eV, CIS: 166.87 eV) peaks indicating the formation of S²⁻ in the samples. ^{13,35} These XPS signals also provide evidence of metal (Zn, Ni, and Cu) sulfur bonds. Based on the above XPS analysis, it was confirmed that Zn2+, Ni2+, Cu+, In3+, and S2- were in the ZnIn2-S₄, NiIn₂S₄, and CuInS₂ catalysts.

The electrochemical activity of ZIS, NIS, and CIS was shown in Fig. 5. The CV curves of the electrocatalysts were obtained at different scan rates (20, 40, 60, 80, 100 mV S⁻¹) within a potential window of -0.5 to 0.5 (Fig. 5a-d). In the case of ZIS and NIS, CV curves were close to rectangular, and it revealed the feature of electric-double layer (EDL) capacitance (Fig. 5a and b). These curves are usually obtained in porous structures, which can suggest continuous electron pathways and promote short ionic transmission distance for enhancement of electrochemical performances.³⁶ A sharp reduction peak was visible in CV curves. NIS showed a higher

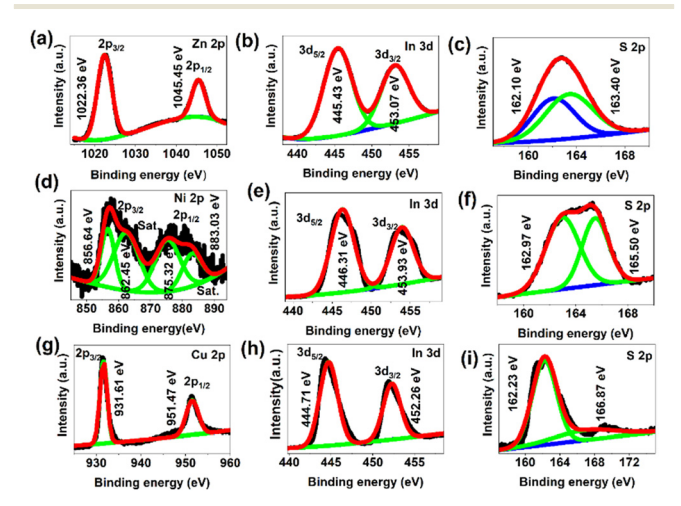


Fig. 4 XPS of ZIS (a: Zn 2p, b: In 3d, and c: S 2p), NIS (d: Ni 2p, e: In 3d, f: S 2p), and CIS (g; Cu 2p, h: In 3d, and i: S 2p).

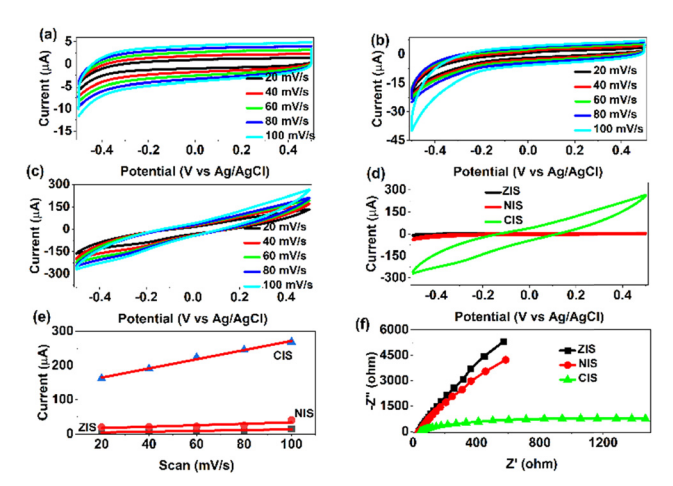


Fig. 5 CV curves of (a) ZIS, (b) NIS, and (c) CIS, (d) combined plot at 100 mV s⁻¹ scan rate, (e) plot of scan rate vs. current, and (f) EIS.

reduction potential/current densities/area than the ZIS. According to Fig. 5c, the non-ideal CV curves were obtained at all scan rates. Also, they deviated from the rectangular shape, which suggests the existence of both non-faradaic reaction/EDL and faradaic reaction. CIS showed higher current densities than ZIS and NIS (Fig. 5a-d). CIS showed 19 and 6-fold enhancement of current density compared to NIS, respectively, indicating the electrocatalytic performance of CuInS2 than those of ZnIn2S4 and NiIn₂S₄.

In all CV curves, current densities increased with an increase in the scan rate, suggesting a good rate performance.³⁷ This may be related to the internal resistance of catalysts and the polarization. The electrochemical performance of CIS compared to ZIS and NIS might be associated with the large surface area and superior pore size, which can provide a greater number of active sites for ion intercalation. The electrochemical surface area (ECSA) was obtained by double layer capacitance (C_{dl}) using various scan rates of electrocatalysts (Fig. 5e). The $C_{\rm dl}$ value of CIS is 1.35 mF cm⁻² which is superior compared to those of NIS (0.21 mF cm⁻²) and ZIS (0.11 mF cm⁻²) electrocatalysts. The exposure of more active sites leads to greater electrochemical performance of the electrocatalyst. The EIS plots are shown in Fig. 5f. According to the Nyquist results, CIS presented a lower impedance than ZIS and NIS. In addition, the equivalent circuit was designed via fitting the AC impedance spectrum (Fig. S5 \dagger). Based on fitting, R_1 (solution resistance), Warburg impedance coefficient (W), R_2 (charge transfer resistance), constant phase element (Q), and double layer capacitance (F) were calculated (Table S1†). CIS showed a lower charge transfer resistance than ZIS and NIS, suggesting superior electrochemical performance via a higher ion diffusion rate as well as great electron transport kinetics on the electrode/electrolyte interface.

To investigate the CO₂RR performances of the electrocatalysts, LSV plots were evaluated. As shown in Fig. 6a, CIS showed higher current densities than ZIS and

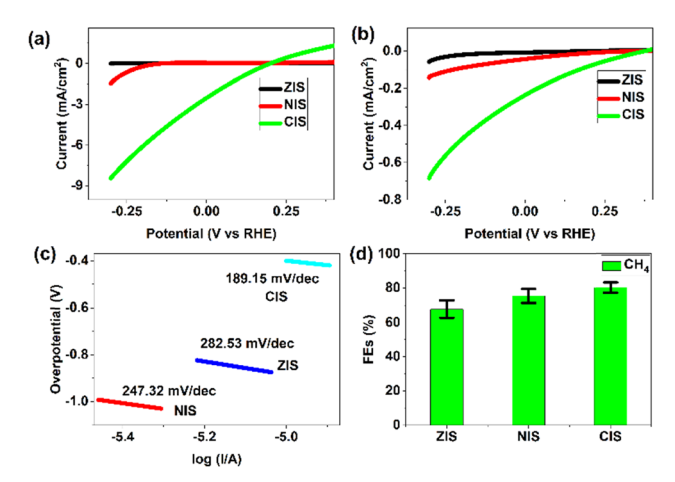


Fig. 6 LSV plots (a) before CO₂ saturation and (b) after CO₂ saturation, (c) Tafel plots, and (d) FEs at -0.6 V versus RHE of ZIS, NIS,

NIS at -0.3 V vs. RHE. CIS demonstrated approximately 5 and 450-fold enhancement of current density as compared to NIS and ZIS, respectively. The current density of ZIS, NIS, and CIS in CO2-saturated 0.1 M KHCO3 indicates a higher current density of CIS than others (Fig. 6b). It also suggests the excellent CO2RR capability of CuInS2 compared to those of ZnIn₂S₄ and NiIn₂S₄. Furthermore, CO₂RR conversion kinetics of the electrocatalysts was further analysed by Tafel plots (Fig. 6c). The Tafel slopes of ZIS, NIS, and CIS were found to be 282.53, 247.32, and 189.15 mV dec⁻¹, respectively. The lowest Tafel slope of CIS indicates the improvement of electrocatalytic activity compared to the others. This result suggests that copper containing metal indium sulfides revealed higher electrocatalytic activity than Ni and Zn-based metal indium sulfides towards the electrocatalytic CO2RR.

To determine the reduction of CO2 into hydrocarbon products electrocatalytically, steady-state current responses of ZIS, NIS, and CIS were evaluated in a CO₂-staurated electrolyte for 400 s at -0.6 V vs. RHE (Fig. S6†). The current densities were -0.45 mA, 0.70 mA, and -1.69 mA for ZIS, NIS, and CIS, respectively. Gaseous and liquid products were obtained while measuring current densities at -0.6 V during the electrocatalytic CO₂RR. The gaseous products were observed by GC, whereas liquid products were determined by 1H NMR (Fig. S7 and Table S2†). As shown in Fig. 6d, FEs for ZIS, NIS, and CIS were 67.78%, 75.31%, and 80.11% towards CH₄ production during the CO2RR, respectively. The result suggests the selective reduction of CO2 into CH4 and superior FE of CuIn2S4 compared to the others during electrochemical reduction. The high electrocatalytic performance of CIS may be attributed to the highly active BET surface area, electrochemical surface area, rich structural design, and good constraints on the active species. In addition, liquid products were analysed by ¹H NMR (Fig. S7†). Two peaks (chemical shift-2.56: DMSO and 4.47: H₂O) appeared in all samples, which indicates the absence of any liquid hydrocarbon products. Furthermore, TOF was

calculated. TOF is one of the key parameters for CO2RR efficiency evaluation. The TOF values of ZIS, NIS, and CIS (-0.6 V versus RHE for 400 s) were $9.5 \times 10^{-3} \text{ s}^{-1}$, $3.1 \times 10^{-2} \text{ s}^{-1}$, and 0.171 s⁻¹, respectively. CIS showed a considerably higher TOF than NIS and ZIS, suggesting superior electrocatalytic CO2RR ability compared to the others.

In addition, Fig. S8† revealed the stability of CuIn2S4 for 20 h at -0.6 V vs. RHE. Also, FEs were calculated after 20 h. The FE of CuIn₂S₄ was 62.53% for CH₄ production during the electrocatalytic reduction of CO2 after 20 h (Fig. S9†). The result revealed that both FE and current density showed only a minor decay over a 20 h period, suggesting significant electrochemical stability of CIS. It also showed evidence of stability towards CH4 generation. By further analyzing the XRD and FESEM images of CIS after the 20 h stability test, it could be found that the phases and morphology were not changed, indicating the excellent stability of CIS (Fig. S10 and S11†). Table 1 presents the comparison of FEs of different catalysts. This table also indicates the comparable electrochemical CO2RR performance of metal (Zn, Ni, and Cu) indium sulfides compared to those from the other published literature works.

According to the mechanism related the electrochemical CO₂RR, the structure/phase of the catalyst determines the adsorption and activation of CO2 molecules.44 Hexagonal, cubic, and tetragonal phases were observed in ZnIn₂S₄, NiIn₂S₄, and CuInS₂, respectively. The (110) plane in metal indium sulfides may enhance the electron cloud between the metal (Zn, Ni, and Cu) atoms and S atoms that can provide electron donation from metals (M) to S atoms. Also, electrons may transfer from In to S atoms. The accumulation of charge around In to S or covalency in the catalyst determines the electrochemical CO₂RR performance.14 The higher electrochemical CO2RR ability of CuInS2 may be associated with higher charge accumulation around In-S bonds. 14,45 Moreover, the interconnected nanosheet structure in the microsphere is beneficial to the exposure of active sites for efficient CO2RR.46

In the case of metal sulfide-based catalysts, the single metal atom sites have a tendency to generate weak bonds with C or O atoms of adsorbed CO2 via hybridization between 2p and 3d orbitals. 47,48 In addition, relatively weak bonds may form between the metal M sites with C or O (M site-C or M site-O) which can be easily cleaved, and CO may be produced during the electrochemical CO₂RR. 49 However, CH₄ was observed using metal (Zn, Ni, and Cu) indium sulfides during the electrochemical CO₂RR. So, dual-metal active sites (In and M) in metal indium sulfides may be responsible for the electrochemical CO₂RR to CH₄. 49 Dual-metal sites can provide highly stable intermediates during the bonding of C and O atoms in the CO2 molecules with two metal sites (Zn or Ni or Cu and In) via hybridization of 2p orbitals of C or O atoms and 3d orbitals of metal atoms. In this case, more energy is required to break the bond between metals and C or O for CO production. In addition, the protonation of C atoms may cause the weakening of the C-O and C-M bond strengths. Due to this reason, CH4 was only observed during the electrochemical CO₂RR of metal indium sulfides. 49-52

Based on CH₄ products during the electrochemical CO₂RR by metal (Zn, Ni, and Cu) indium sulfides, the reaction pathways were proposed. At first, the protonation of *CO to *CHO is the potential determining step and the ratedetermining step. The intermediate CO products are highly endergonic on metal indium sulfide catalysts, which may cause the generation of CO to be virtually prohibited. Also, hydrogen evolution may be prohibited. During this step, metal-indium dual sites may form stronger bonds with *CHO which can lower the energy barrier. Then, *CHO may produce *CH₃O species because of various proton-electron coupled reactions. In this step, the stronger metal-oxygen bonds on the surface of metal indium sulfides may provide easier weakening and breakage of the CH₃O group because of intense hybridization between the d-orbital of the metals and the p-orbital of oxygen atoms. Also, introducing Cu, Ni, and Zn in metal indium sulfides may stabilize the *CH₃O intermediate and breakage of the C-O bond. Finally, CH4 is produced on the surface of metal indium sulfide by breaking the C-O bond of *CH₃O.^{5,10,49,53,54}

Conclusions

In summary, nanosheet assembled metal indium sulfides (ZnIn₂S₄, NiIn₂S₄, and CuInS₂) were synthesized using a hydrothermal method for selective electrochemical reduction

Table 1 Comparison of CH₄ conversion FEs of various electrocatalysts during electrocatalytic CO₂RR based on the published literature

| Catalyst | Synthesis method | Morphology | FEs -CH ₄ (%) | Potential (V vs. RHE/SCE) | References |
|---|-----------------------------|----------------------------------|----------------------------|------------------------------|------------|
| Cu-CeO ₂ | Hydrothermal | Nanorods | 49.3 | -1.6 | 38 |
| Ag-Cu ₂ O | Wet chemical reduction | Hollow nanospheres | 62 | -1.5 | 39 |
| N-doped C/Cu | Calcination | Nanoparticles | 30 | -1.65 | 40 |
| OH-AAn-COF-Cu | Shiff-base condensation | Nanofibers | 77 | -1 | 41 |
| MWCNT-Por-COF-Cu | Mixing/heating/solvothermal | Nanotubes | 71.2 | -0.7 | 42 |
| Cu ₂ O/MOF | Electrochemical treatment | Nanoparticles | 73 | -1.4 | 43 |
| Cu/MOF | Solvothermal | Rods | 80 | -0.9 | 6 |
| Cu porphyrin | Chemical | Irregular | 54.8 | -1.63 | 7 |
| Cu/CeO ₂ | Wet impregnation | Layered | 15 | -0.89 | 9 |
| ZnIn ₂ S ₄ , Niin ₂ S ₄ , and CuIns ₂ | Hydrothermal | Nanosheet assembled microspheres | 67.78, 75.31, and 80.11 | -0.6 | Our work |

of CO₂ into CH₄. The electrochemical characterization (CV, ESCA, EIS, LSV, chronoamperometry, and Tafel plot) of catalysts was performed, which indicated the excellent electrochemical performance of CuInS2 compared to those of ZnIn₂S₄ and NiIn₂S₄. CuInS₂ exhibited a higher CH₄ FE of 80.11% at -0.6 V vs. RHE than other catalysts (ZnIn₂S₄: 67.78% and NiIn₂S₄: 75.31%) in an H-type cell. Also, CuInS₂ showed a higher TOF than others. The high selectivity for reducing CO2 to CH4 by metal indium sulfide electrocatalysts was attributed to great active sites, high BET surface area, excellent electrochemical surface area, and good structural design. Moreover, the catalyst demonstrated remarkable stability during the electrochemical reduction reaction for 20 h without lowering the current density. The stability of the catalyst was further supported by XRD and FESEM analysis after the electrochemical CO₂RR. The possible mechanisms/ pathways were proposed. This work may inspire new exploration and design of stable metal indium sulfides for highly selective electroreduction of CO2 into CH4.

Data availability

The authors declare that the data supporting this study are available within the main text and its ESI.† Should any raw data files be needed in another format, they are available from the corresponding author upon reasonable request.

Author contributions

Schindra Kumar Ray: conceptualization, methodology, validation, formal analysis, investigation, data curation, writing – original draft, review, and editing; Rabin Dahal: FESEM images; Moses D. Ashie: XPS measurement; Gayani Pathiraja: TEM images; Bishnu Prasad Bastakoti: funding acquisition, resources, supervision, and writing – review & editing.

Conflicts of interest

There are no conflicts to declare.

Acknowledgements

The National Science Foundation's Excellence in Research Award (2100710) USA supported this research. Some of the characterization was performed in the Joint School of Nanoscience and Nanoengineering, a member of the Southeastern Nanotechnology Infrastructure Corridor and National Nanotechnology Coordinated Infrastructure, which is supported by the National Science Foundation (Grant ECCS-1542174). The authors thank Professor Mufeed Basti for the BET measurement.

Notes and references

1 H. Wang, Y. K. Tzeng, Y. Ji, Y. Li, J. Li, X. Zheng, A. Yang, Y. Liu, Y. Gong, L. Cai, Y. Li, X. Zhang, W. Chen, B. Liu, H. Lu,

- N. A. Melosh, Z. X. Shen, K. Chan, T. Tan, S. Chu and Y. Cui, *Nat. Nanotechnol.*, 2020, **15**, 131–137.
- 2 S. K. Ray, R. Dahal, M. D. Ashie and B. P. Bastakoti, *Sci. Rep.*, 2024, 14, 1406.
- 3 T. Zhang, H. Shang, B. Zhang, D. Yan and X. Xiang, ACS Appl. Mater. Interfaces, 2021, 13, 16536–16544.
- 4 T. Gao, A. Kumar, Z. Shang, X. Duan, H. Wang, S. Wang, S. Ji, D. Yan, L. Luo, W. Liu and X. Sun, *Chin. Chem. Lett.*, 2019, **30**, 2274–2278.
- 5 J. Cai, Q. Zhao, W. Y. Hsu, C. Choi, Y. Liu, J. M. P. Martirez, C. Chen, J. Huang, E. A. Carter and Y. Huang, *J. Am. Chem. Soc.*, 2023, 145, 9136–9143.
- 6 Y. Zhang, L. Z. Dong, S. Li, X. Huang, J. N. Chang, J. H. Wang, J. Zhou, S. L. Li and Y. Q. Lan, *Nat. Commun.*, 2021, 12, 1–9.
- 7 P. Yu, X. Lv, Q. Wang, H. Huang, W. Weng, C. Peng, L. Zhang and G. Zheng, *Small*, 2023, **19**, 1–7.
- 8 M. Umeda, Y. Yoshida and S. Matsuda, *Electrochim. Acta*, 2020, **340**, 135945.
- 9 K. K. Patra, Z. Liu, H. Lee, S. Hong, H. Song, H. G. Abbas, Y. Kwon, S. Ringe and J. Oh, ACS Catal., 2022, 10973-10983.
- 10 L. Han, S. Song, M. Liu, S. Yao, Z. Liang, H. Cheng, Z. Ren, W. Liu, R. Lin, G. Qi, X. Liu, Q. Wu, J. Luo, H. L. Xin, X. Liu, Q. Wu, J. Luo and H. L. Xin, J. Am. Chem. Soc., 2020, 142, 12563–12567.
- 11 F. Cai, X. Hu, F. Gou, Y. Chen, Y. Xu, C. Qi and D. K. Ma, *Appl. Surf. Sci.*, 2023, **611**, 155696.
- 12 G. Zhang, H. Wu, D. Chen, N. Li, Q. Xu, H. Li, J. He and J. Lu, *Green Energy Environ.*, 2022, 7, 176–204.
- 13 L. Wang, B. Cheng, L. Zhang and J. Yu, *Small*, 2021, 17, 1–9.
- 14 L. P. Chi, Z. Z. Niu, X. L. Zhang, P. P. Yang, J. Liao, F. Y. Gao, Z. Z. Wu, K. Bin Tang and M. R. Gao, *Nat. Commun.*, 2021, 12, 1–9.
- 15 L. Wu, L. Wu, C. Guo, Y. Guan, H. Wang and J. Lu, *Processes*, 2023, 11, 1039.
- 16 S. He, D. Ji, J. Zhang, P. Novello, X. Li, Q. Zhang, X. Zhang and J. Liu, J. Phys. Chem. B, 2020, 124, 511–518.
- 17 Y. He, H. Rao, K. Song, J. Li, Y. Yu, Y. Lou, C. Li, Y. Han, Z. Shi and S. Feng, *Adv. Funct. Mater.*, 2019, **29**, 1–10.
- 18 M. N. Hossain, P. Prslja, C. Flox, N. Muthuswamy, J. Sainio, A. M. Kannan, M. Suominen, N. Lopez and T. Kallio, *Appl. Catal.*, B, 2022, 304, 120863.
- 19 Z. Zhang, K. Liu, Z. Feng, Y. Bao and B. Dong, *Sci. Rep.*, 2016, 6, 1–10.
- 20 J. Xia, Q. Wang, M. Wei, L. Chen, N. Liu, S. Fan and H. Wu, J. Mater. Sci., 2021, 56, 2372–2384.
- 21 A. Wang, H. Liang, F. Chen, X. Tian, S. Yin, S. Jing and P. Tsiakaras, *Appl. Catal.*, *B*, 2022, **310**, 121336.
- 22 J. Ning, S. V. Kershaw and A. L. Rogach, J. Am. Chem. Soc., 2019, 141, 20516–20524.
- 23 D. Pan, L. An, Z. Sun, W. Hou, Y. Yang, Z. Yang and Y. Lu, *J. Am. Chem. Soc.*, 2008, **130**, 5620–5621.
- 24 X. Yin, B. Lv, Y. Kang, X. Xu, X. Lei, L. Li, H. Wang, H. Xi, J. Yang and Z. Yang, *Catal. Lett.*, 2023, **153**, 570–583.

- 25 Z. Chen, D. Li, W. Zhang, C. Chen, W. Li, M. Sun, Y. He and X. Fu, Inorg. Chem., 2009, 40, 9766-9772.
- 26 D. Wang, M. Cao, Y. Feng and J. Yao, Microporous Mesoporous Mater., 2022, 330, 111598.
- 27 S. Sun, H. Cheng, X. Li, X. Wu, D. Zhen, Y. Wang, R. Jin and G. He, Ind. Eng. Chem. Res., 2021, 60, 1164-1174.
- 28 B. R. KC, D. Kumar and B. P. Bastakoti, J. Mater. Sci., 2024, 59, 10193-10206.
- 29 S. K. Ray, D. Dhakal, J. Hur and S. W. Lee, Nanotechnology, 2019, 31, 084002.
- 30 S. K. Ray, R. Prasad Pandey, S. Jeong and S. Lee, I. Photochem. Photobiol., A, 2018, 367, 162-170.
- 31 S. K. Ray, D. Dhakal, G. Gyawali, B. Joshi, A. Raj Koirala and S. W. Lee, Chem. Eng. J., 2019, 373, 259-274.
- 32 S. Kumar Ray, P. Anil Kumar Reddy, S. Yoon, J. Shin, K. Chon and S. Bae, Chem. Eng. J., 2023, 452, 139546.
- 33 M. A. Mushtaq, A. Kumar, G. Yasin, M. Tabish, M. Arif, S. Ajmal, W. Raza, S. Naseem, J. Zhao, P. Li, H. G. Ali, S. Ji and D. Yan, Small, 2024, 2310431, 1-12.
- 34 X. Fu, J. Tao, Z. Zhao, S. Sun, L. Zhao, Z. He, Y. Gao and Y. Xia, RSC Adv., 2023, 13, 8227-8237.
- 35 M. A. Mushtaq, A. Kumar, G. Yasin, M. Arif, M. Tabish, S. Ibraheem, X. Cai, W. Ye, X. Fang, A. Saad, J. Zhao, S. Ji and D. Yan, Appl. Catal., B, 2022, 317, 121711.
- 36 H. Guo, Z. Liu, H. Li, H. Wu, C. Zhang, J. Yang and X. Chen, Appl. Phys. A: Mater. Sci. Process., 2017, 123, 1-9.
- 37 S. K. Ray and B. P. Bastakoti, Int. J. Hydrogen Energy, 2024, 51, 1109-1118.
- 38 L. Xue, C. Zhang, J. Wu, Q. Y. Fan, Y. Liu, Y. Wu, J. Li, H. Zhang, F. Liu and S. Zeng, Appl. Catal., B, 2022, 304, 120951.
- 39 M. Sun, L. Zhang, F. Tian, J. Li, Y. Lei, H. Zhang, L. Han, Z. Guo, Y. Gao, F. Liu, Y. Wang, L. Wang and S. Zeng, J. Energy Chem., 2024, 88, 521-531.

- 40 C. J. Jiang, Y. Hou, H. Liu, L. T. Wang, G. R. Zhang, J. X. Lu and H. Wang, J. Electroanal. Chem., 2022, 915, 116353.
- 41 M. Liu, Y. R. Wang, H. M. Ding, M. Lu, G. K. Gao, L. Z. Dong, Q. Li, Y. Chen, S. L. Li and Y. Q. Lan, Sci. Bull., 2021, 66, 1659-1668.
- 42 H. Dong, M. Lu, Y. Wang, H. L. Tang, D. Wu, X. Sun and F. M. Zhang, Appl. Catal., B, 2022, 303, 120897.
- 43 J. Yi, R. Xie, Z. Xie, G. Chai, T. Liu, R. Chen, Y. Huang and R. Cao, Angew. Chem., 2020, 132, 23849-23856.
- 44 J. Yang, Z. Yang, K. Yang, Q. Yu, X. Zhu, H. Xu and H. Li, Chin. J. Catal., 2023, 44, 67-95.
- 45 W. Tao, C. Zhu, Q. Xu, S. Li, X. Xiong, H. Cheng, X. Zou and X. Lu, ACS Omega, 2020, 5, 20090-20099.
- 46 J. Zhao, Z. Xiong, Y. Zhao, X. Chen and J. Zhang, Environ. Res., 2023, 216, 114699.
- 47 S. Wang, B. Y. Guan, Y. Lu and X. W. Lou, J. Am. Chem. Soc., 2017, 139, 17305-17308.
- 48 K. K. Ghuman, L. B. Hoch, P. Szymanski, J. Y. Y. Loh, N. P. Kherani, M. A. El-Saved, G. A. Ozin and C. V. Singh, J. Am. Chem. Soc., 2016, 138, 1206-1214.
- 49 X. Li, Y. Sun, J. Xu, Y. Shao, J. Wu, X. Xu, Y. Pan, H. Ju, J. Zhu and Y. Xie, Nat. Energy, 2019, 4, 690-699.
- 50 Y. Sun, S. Gao and Y. Xie, Chem. Soc. Rev., 2014, 43, 530-546.
- 51 S. Sorcar, J. Thompson, Y. Hwang, Y. H. Park, T. Majima, C. A. Grimes, J. R. Durrant and S. Il In, Energy Environ. Sci., 2018, 11, 3183-3193.
- 52 K. L. Bae, J. Kim, C. K. Lim, K. M. Nam and H. Song, Nat. Commun., 2017, 8, 1-8.
- 53 J. Zhao, P. Zhang, T. Yuan, D. Cheng, S. Zhen, H. Gao, T. Wang, Z. J. Zhao and J. Gong, J. Am. Chem. Soc., 2023, 145, 6622-6627.
- 54 Z. Sun, T. Ma, H. Tao, Q. Fan and B. Han, Chem, 2017, 3, 560-587.